Raman Spectroscopic Features of the Neutral Vacancy in Diamond from Ab Initio Quantum-mechanical Calculations

Noname manuscript No.
(will be inserted by the editor)

Spectroscopic Vibrational Features of the Neutral Vacancy in Diamond from Quantum-mechanical Calculations

Alessandro Zelferino[1] · **Paolo Olivero**[2] · **Jacopo Baima**[1] · **ZIZI** [1] · **Alessandro Erba**[1] · **Roberto Dovesi**[1]

Received: date / Accepted: date

Abstract The vibrational spectrum of the neutral vacancy in diamond is investigated by using a periodic approach (supercells including 32, 64, 128 and 256 atoms have been considered), a "hybrid" functional (B3LYP), and a local basis set as implemented in the CRYSTAL14 code. The Raman spectrum, that shows a single peak in the perfect bulk (at 1333 cm^{-1} from our simulation, in excellent agreement with the experimental result at 1332 cm^{-1}), presents a complex structure at lower frequencies (from 200 cm^{-1} to the bulk peak) when the defect is present. The details of this structure are changing with the concentration of the defects. The IR spectrum (that is completely flat in perfect diamond) shows a fine structure with intensities that are however very low, not easily detectable in the experiment. The ADP (Atomic Displacement Parameters), representing the mean displacement of the atoms as a consequence of their vibration, show how the first neighbors are elongated along the defect direction (the principal axis is nearly twice the two others along the orthogonal directions), and how the nearly spherical shape of the "unperturbed" bulk atoms is recovered at the third-fourth neighbors. The difference in the vibrational DOS between the perfect and defective system completes the analysis.

Keywords Vacancy in diamond · Raman Spectrum · IR Spectrum · Atomic Displacement Parameters · Quantum Mechanical Calculation · CRYSTAL code · Hybrid Functionals

[1] Dipartimento di Chimica, Università di Torino and NIS (Nanostructured Interfaces and Surfaces) Centre, Via P. Giuria 5, 10125 Torino, Italy

[2] Dipartimento di Fisica, Università di Torino, Via P. Giuria 1, 10125 Torino, Italy

1 Introduction

Since many years, the investigation of native and radiation-induced point defects in semiconductors has attracted an ever-increasing interest in both theoretical and experimental studies. This is particularly true in the case of diamond, a wide-bandgap material characterized by extreme physical properties (high Young's modulus and thermal conductivity, broad transparency range, high carriers mobility, etc.) with attractive applications in different fields, ranging from microelectromechanical systems to heatsinks, laser windows, particle detectors, etc. [1,2]. Indeed, the presence of defects in the crystal structure of diamond has a dramatic effect on its physical properties, from a structural [3], optical [4] and electronic [5] point of view. A deep understanding of the physical effects of different typologies of defects is therefore of paramount importance in modern diamond science. Despite a large number of studies on the subject [6–11], the defect formation in diamond is still far from having been exhaustively explored. This is particularly due to the peculiar metastability of its crystalline structure, in which the both sp^3 and graphitic-like sp^2 chemical bonds give rise to an unusual variety of different point defects and related complexes. Raman spectroscopy is the ideal technique to study different carbon allotropes due to their characteristic vibrational features [12, 13], and in this context it emerged as a prominent technique to investigate defect formation in irradiated diamond [14–16,6,7,17,11,18–21]. The Raman spectrum of pristine diamond only displays a single sharp Raman feature at 1332 cm^{-1}, corresponding to the first-order scattering with triply-degenerated TO(X) phonons of F_{2g} symmetry, while the damaged crystal is characterized by several additional features which have been more or less unequivocably attributed to different types of sp^2 and sp^3 defects. The most prominent features observed at higher Raman frequencies with respect to the first-order line are located at $\sim 1450\ cm^{-1}$, $\sim 1490\ cm^{-1}$, $\sim 1630\ cm^{-1}$ and $\sim 1680\ cm^{-1}$. They are generally attributed to sp^2 defects [22], although tenative attributions of the $\sim 1450\ cm^{-1}$ and $\sim 1490\ cm^{-1}$ peaks to sp^3 defects have also been formulated [16,20]. At lower Raman frequencies, a broad band of peaks are usually measured between $\sim 1100\ cm^{-1}$ and $\sim 1300\ cm^{-1}$ shifts, whose attribution is more unclear [22]. Moreover, the first-order Raman peak itself is subjected to both broadening and red-shifting when damage is introduced in the crystal [14].

2 Computational Methods and Details

2.1 Spectroscopic Features

Harmonic phonon frequencies, ω_p, at the Γ point (*i.e.* at the center of the first Brillouin zone, FBZ, in reciprocal space) are obtained from the diagonalization of the mass-weighted Hessian matrix of the second energy derivatives with

respect to atomic displacements u [23–25]:

$$W^{\Gamma}_{ai,bj} = \frac{H^{\mathbf{0}}_{ai,bj}}{\sqrt{M_a M_b}} \quad \text{with} \quad H^{\mathbf{0}}_{ai,bj} = \left(\frac{\partial^2 E}{\partial u^{\mathbf{0}}_{ai} \partial u^{\mathbf{0}}_{bj}} \right) , \tag{1}$$

where atoms a and b (with atomic masses M_a and M_b) in the reference cell, $\mathbf{0}$, are displaced along the i-th and j-th Cartesian directions, respectively. First order derivatives are computed analytically, whereas second order derivatives are obtained numerically, using a two-point formula.

The Raman intensity of the Stokes line of a phonon mode Q_p, active due to the $\alpha_{ii'}$ component of the polarizability tensor α, is given by:

$$I^{p}_{ii'} \propto \left(\frac{\partial \alpha_{ii'}}{\partial Q_p} \right)^2 , \tag{2}$$

where the pre-factor dependent on the laser frequency ω_L and temperature T [26] is neglected. The relative Raman intensities of the peaks are computed analytically by exploiting a scheme, recently implemented in the CRYSTAL14 program [27,28], which constitutes an extension of the analytical calculation of IR intensities [29,30]. Both schemes are based on the solutions of first- and second-order Coupled-Perturbed-Hartree-Fock/Kohn-Sham (CPHF/KS) equations [31,32].

The Raman spectrum is computed by considering the transverse optical (TO) modes and by adopting a pseudo-Voigt functional form: a linear combination of a Lorentzian and a Gaussian curve with full width at half maximum of 8 cm^{-1}. Raman intensities are normalized so that the largest value is conventionally set to 1000 a.u. Integrated intensities for IR absorption are computed for each mode by means of the mass-weighted effective mode Born charge vector, evaluated through a Berry phase approach [33–35].

2.2 Phonon Dispersion and Thermodynamic Properties

The calculation of other vibrational properties of solids (such as thermodynamic quantities or thermal nuclear motion indices) is a more demanding task as it implies knowledge of the phonon dispersion inside the full FBZ [36]. Beside $\mathbf{W}^{\Gamma}$, in this case, a set of dynamical matrices, $\mathbf{W}^{\mathbf{k}}$, need to be formed for a set of wavevectors $\mathbf{k} = \sum_i \frac{\kappa_i}{L_i} \mathbf{b}_i$ expressed as linear combinations of reciprocal lattice basis vectors $\mathbf{b}_i$ with fractional coefficients referred to shrinking factors L_i, κ_i being an integer ranging from 0 to $L_i - 1$, thus including Γ and points within the FBZ. Phonons at $\mathbf{k}$ points other than Γ can be obtained by the *direct method* [37–39], which requires the construction of supercells (SC) of the original unit cell:

$$W^{\mathbf{k}}_{ai,bj} = \sum_{\mathbf{g} \in SC} \frac{H^{\mathbf{g}}_{ai,bj}}{\sqrt{M_a M_b}} \, e^{\imath \mathbf{k} \cdot \mathbf{g}} \, . \tag{3}$$

Indeed, equation (3) shows that each dynamical matrix in the FBZ is obtained by Fourier transforming the Hessian matrices, $\mathbf{H^g}$, for an adequate set of real space lattice vectors $\mathbf{g}$. Lattice vectors $\mathbf{g} = \sum_i l_i^g \, \mathbf{a}_i$, expressed in terms of the real lattice basis vectors $\{\mathbf{a}_i\}$ through the integer coefficients l_i^g, are all contained in the SC in real space whose size and shape are determined by parameters L_i. At variance with equation (1), matrix element $H^{\mathbf{g}}_{ai,bj} = \partial^2 E/(\partial u^{\mathbf{0}}_{ai} \partial u^{\mathbf{g}}_{bj})$ refers to a displacement of atom b in cell $\mathbf{g}$ inside the SC along the Cartesian direction j, along with all its images throughout the superlattice generated by the SC. L_i are the same both in the real and the reciprocal space so as to maintain a one-to-one matching between $\mathbf{g}$ vectors in the SC and sampled $\mathbf{k}$ points. From diagonalization of the dynamical matrices the normal modes and corresponding vibration frequencies are sampled over the entire FBZ:

$$(\mathbf{U^k})^\dagger \, \mathbf{W^k} \, \mathbf{U^k} \; = \; \mathbf{\Lambda^k} \quad \text{with} \quad (\mathbf{U^k})^\dagger \mathbf{U^k} = \mathbf{I} \, . \tag{4}$$

The elements of the diagonal $\mathbf{\Lambda^k}$ matrix provide the *vibrational frequencies*, $\nu_{\mathbf{k}p} = \sqrt{\lambda_{\mathbf{k}p}}$ (atomic units are adopted), while the columns of the $\mathbf{U^k}$ matrix contain the corresponding *normal coordinates* $\mathbf{u^k_p}$ (whose elements are $u^{\mathbf{k}}_{ia,p}$, being ia a combined index running from 1 to $3M$, where M is the number of atoms per cell). To each $\mathbf{k}$-point in the first Brillouin zone, $3M$ harmonic oscillators (*i.e.* phonons) are associated, which are labeled by a phonon band index p ($p = 1, \ldots, 3M$) and whose energy levels are given by the usual harmonic expression:

$$\varepsilon_m^{p,\mathbf{k}} = \left(m + \frac{1}{2} \right) \omega_{\mathbf{k}p} \, , \tag{5}$$

where m is an integer and $\omega_{\mathbf{k}p} = 2\pi\nu_{\mathbf{k}p}$. According to standard statistical mechanics, thermodynamic properties of crystalline materials such as entropy, $S(T)$, and constant-volume specific heat, $C_V(T)$, can be expressed as [40]:

$$S(T) = k_B \sum_{\mathbf{k}p} \left[\frac{\hbar\omega_{\mathbf{k}p}}{k_B T \left(e^{\frac{\hbar\omega_{\mathbf{k}p}}{k_B T}} - 1 \right)} - \log(1 - e^{-\frac{\hbar\omega_{\mathbf{k}p}}{k_B T}}) \right] \, , \tag{6}$$

$$C_V(T) = \sum_{\mathbf{k}p} \frac{(\hbar\omega_{\mathbf{k}p})^2}{k_B T^2} \frac{e^{\frac{\hbar\omega_{\mathbf{k}p}}{k_B T}}}{\left(e^{\frac{\hbar\omega_{\mathbf{k}p}}{k_B T}} - 1 \right)^2} \, , \tag{7}$$

where k_B is Boltzmann's constant.

2.3 Atomic Thermal Motion

Atomic anisotropic displacement parameters (ADPs) are commonly adopted to discuss mean square atomic displacements due to thermal nuclear motion, particularly so in the field of X-ray diffraction. Due to zero-point and thermal motion, indeed, each atom has a finite probability of being displaced with

respect to its crystallographic equilibrium position. ADPs offer a convenient way to rationalize such atomic motions; to each atom and for any temperature, an ellipsoid is associated, which provides information on the probability of finding that atom displaced from the equilibrium position. Atomic ADPs can be given a 3×3 Cartesian matrix representation according to [39,41]:

$$B^a_{ij}(T) = \frac{1}{n_k M_a} \sum_{p\mathbf{k}} \frac{\mathcal{E}_{p\mathbf{k}}(T)}{\omega^2_{p\mathbf{k}}} e^{\mathbf{k}}_{ia,p} \times (e^{\mathbf{k}}_{ja,p})^* \tag{8}$$

where the sum runs over phonons in the FBZ and $\mathcal{E}_{p\mathbf{k}}(T)$ is the mean vibrational energy of a phonon (*i.e.* harmonic oscillator) with angular frequency $\omega_{p\mathbf{k}}$, in thermal equilibrium at temperature T [42]:

$$\mathcal{E}_{p\mathbf{k}}(T) = \hbar\omega_{p\mathbf{k}} \left[\frac{1}{2} + \frac{1}{e^{\frac{\hbar\omega_{p\mathbf{k}}}{k_B T}} - 1} \right] . \tag{9}$$

If $\mathbf{B}^a(T)$ is positive definite then the surfaces of constant probability defined by

$$\mathbf{u}_a^T \mathbf{B}^a(T)^{-1} \mathbf{u}_a = \text{constant} , \tag{10}$$

are *ellipsoids* enclosing some finite probability for atomic displacement [43]. The length of the principal semi-axes of the ellipsoid and their orientation are given by the eigenvalues and eigenvectors of $\mathbf{B}^a(T)$, respectively. The eigenvalues λ_i are usually expressed in units of 10^{-4} Å^2. Present calculations refer to harmonic ADPs, which correspond to a constant-volume case. In order to account for thermal changes in the cell volume, a quasi-harmonic approximation could be used instead [42,40,44–46].

2.4 Computational Setup

All calculations have been performed within unrestricted density functional theory (DFT) using the B3LYP hybrid functional [47], as implemented in the CRYSTAL14 program [48,49]. A Pople's 6-21G Gaussian basis set [50] has been adopted, the exponent of the most diffuse *sp* shell having been re-optimized in bulk diamond (0.2279 Å^{-2}). The same basis set is centered at the vacancy position to increase the variational freedom around the defect. The truncation of the Coulomb and exchange infinite series is controlled by five parameters, which have been set to 8, 8, 8, 8, 16. The convergence threshold on energy for the self-consistent-field (SCF) calculations is 10^{-8} Ha for structural optimization and 10^{-9} for vibration frequency calculations. Reciprocal space has been sampled using a regular sublattice with shrinking factor of 16 (or 8, 4) for supercells containing 2 (or 8, $\geq$ 64) atoms, respectively. The number of corresponding **k**-points in the irreducible part of the Brillouin zone is 145 (or 29, 10), respectively when the full symmetry of the diamond lattice is preserved.

A supercell approach is used to simulate the neutral vacancy, where a large periodic cell is created, which is a multiple of the unit cell of the perfect system,

and an atom is removed at its center to create the defect. This scheme allows to effectively investigate the variation of any property with increasing defect concentration. Supercells containing a number of carbon atoms ranging from 32 to 216 (before the vacancy creation) have been considered.

3 Results

Experimentally, different allotropic forms of carbon are widely investigated by Raman spectroscopy [51]. The non defective diamond Raman spectrum is widely known and displays a single prominent peak at ν=1332 cm^{-1}. The peak frequency in the Raman spectrum depends principally on the bond length and strength: as the inter-atomic distance increases the Raman shift frequency lowers. The vacancy distorts the cell and then its nearest and next nearest neighbors undergo relaxation. This affects the bond lenghts and as a consequence the Raman spectrum. As different symmetries around the defect are provided by different spin states, we investigate the effect of this feature on the Raman spectrum. In particular the S_z=0,1 spin states will be considered. We neglect the S_z=2 spin state since we want to consider only the ground state of the system and the first excited state.

The B3LYP Hamiltonian is adopted, that provides good results in the calculation of chemical properties such as vibrational frequencies [52–54]. The non-defective diamond peak is at ν=1333 cm^{-1} (ν=1332 cm^{-1} is the experimental value). Vibrational frequencies at k$\neq \Gamma$ are Raman inactive.

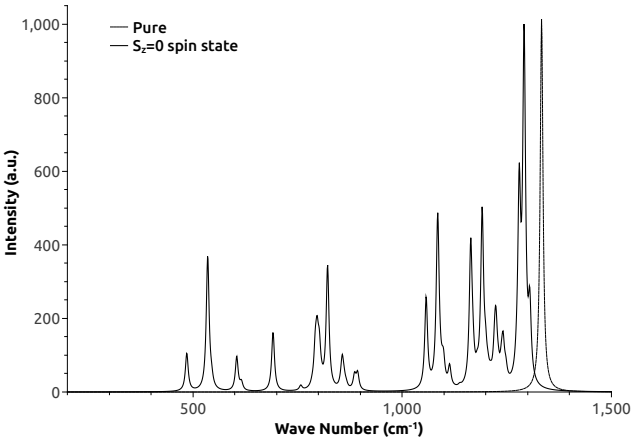

Fig. 1 Raman spectra of non-defective and damaged diamond. The Raman spectrum of the S_z=0 spin state in the S_{32} supercell is used for comparison. The dashed peak is the one of the non-defective system. The wave number range varies from 200 cm^{-1} to 1500 cm^{-1}.

As mentioned above, the presence of the defect breaks the traslational symmetry of non-defective diamond and reduces the point symmetry, so that more

peaks emerge as can be seen in the figure 1 where we report a comparison between the Raman spectra of the non-defective diamond and of the defective diamond in the S_z=0 spin solution. Some vibrational frequencies are similar to k$\neq \Gamma$ of non-defective diamond (not shown here because they are Raman inactive), others are entirely new features. Let us consider, for example, the low-energy part of the spectrum: in the non-defective system the lowest mode is at ν=661 cm^{-1} (not shown in figure 1 because it is Raman inactive) whereas a large acoustic band between ν=485 cm^{-1} and ν=647 cm^{-1} appears in the spectrum of the defective system. Our model predicts 90 Raman active frequencies for the Raman spectrum of the S_z=0 state for neutral vacancy in the S_{32} supercell. Most of them have low intensities so we refer only to the most relevant ones.

Figure 2 shows the Raman spectra of the S_{32} supercell in the S_z=0 and S_z=1 spin states. The vibrational frequencies of the two systems are quite similar whereas the Raman intensities of each peak are slighly different. The most intense peak of the S_z=1 state is at ν=1306 cm^{-1} and a similar vibrational frequency (ν=1304 cm^{-1} occurs for the S_z=0). The S_z=0 principal mode at ν=1291 cm^{-1} appears also as a S_z=1 mode at ν=1293 cm^{-1} but it turns out to be Raman inactive (note: the two states have different point group symmetries, i.e. C_{2v} for the S_z=0 and C_{3v} for the S_z=1).

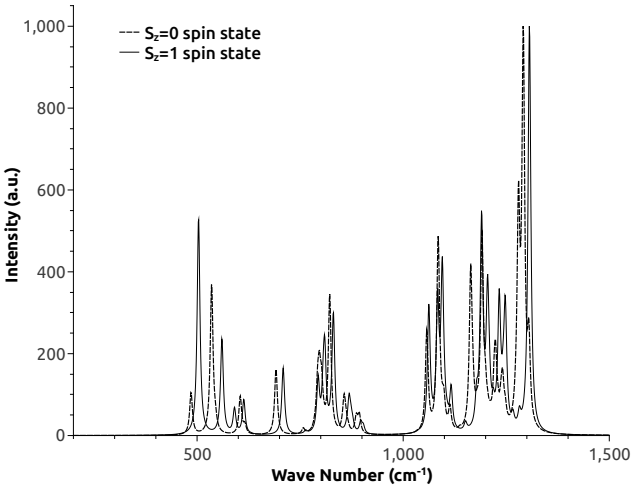

Fig. 2 Comparison between the Raman spectra relevant to the S_z=1 and S_z=0 spin states of the vacancy. The S_{32} supercell is used as a reference. The wave number range varies from 200 cm^{-1} to 1500 cm^{-1} .

We also considered the evolution of the Raman spectra with the concentration of defects. The S_{32} - S_{128} supercell range in the S_z=0 spin state has been analyzed (figure 3). The main Raman line at ν=1291 cm^{-1} of the S_{32} supercell shifts to ν=1314 cm^{-1} in the S_{64} supercell, and to ν=1324 cm^{-1} in the S_{128} one approaching the non-defective system at ν=1333 cm^{-1}. This dif-

ference (1324 - 1333) can be considered as a measure of the residual interaction among defects in the S_{128} supercell.

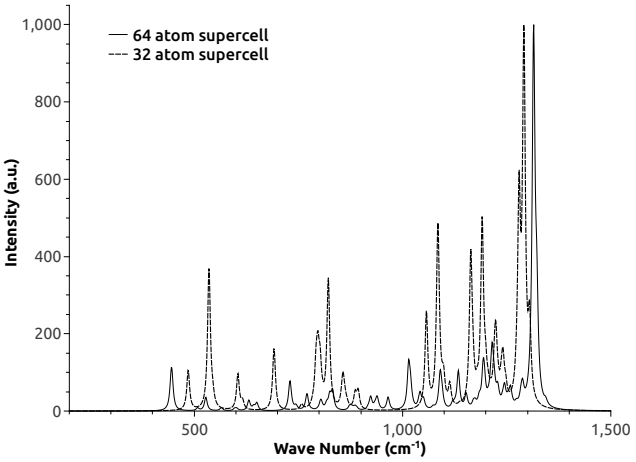

Fig. 3 The Raman spectra of the vacancy in the S_z=0 spin state in the S_{32} and S_{64} supercells. The wave number range varies from 200 cm^{-1} to 1500 cm^{-1} .

The fact that the most intense Raman peak descreases in frequency with increasing the density of defect is experimentally verified [55]. The authors report in [55] a linear depedence of the Raman peak position in a damaged diamond as function of the ion irradiation fluence. We convert the fluence into the defects density by using the **TRIM** [56] code to make a comparison between our calculated data and the experimental results.

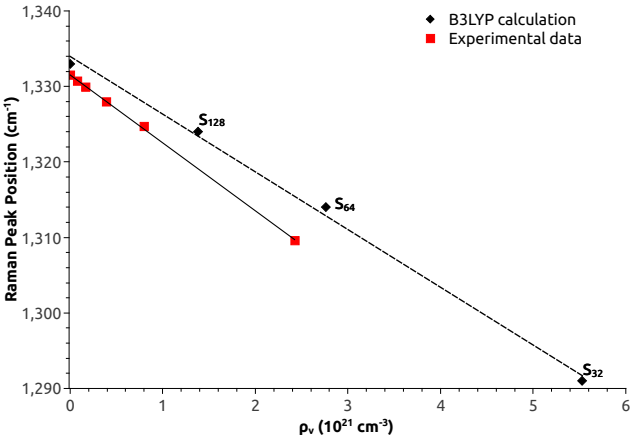

Fig. 4 First order Raman peak position as a function of the density of defects .

Figure 4 shows the linear fits of experimental and calculated data. Slopes are reasonably similar, although not compatible from a strictly statistical point of view:

$$\Delta p_{th} = (\text{-}7.64\pm0.30)\ 10^{21}\text{cm}^{-2}$$
$$\Delta p_{exp} = (\text{-}8.99\pm0.11)\ 10^{21}\text{cm}^{-2}$$

The experimental Raman peak position decreases more rapidly than the calculated one. This is probably due to the presence of other types of defects (i.e. aggregation of vacancies-interstitials) in the defective material.

We try now to identify the vibrational modes which principally involve the four n.n. of the vacancy. To do this, we perform an isotopic substitution of these atoms. This practice is very common in the study of molecular vibrational properties and provides good information about atoms involved in specific normal modes. It consists in replacing atoms with one of their isotopes and compare the resulting spectra.
In the simulation we can change atomic masses by any amount with no necessary reference to any existing nuclear isotopes. This makes it possible to identify which vibrational frequencies are mainly affected by this modification, i.e. which atoms are mainly involved in the vibration mode.

We remind that the dynamic matrix W is defined in terms of the hessian matrix $H_{ai,bj}$ as follows

$$W_{ai,bj} = \frac{H_{ai,bj}}{\sqrt{M_a M_b}} \tag{11}$$

Equation 11 shows that when increasing a mass, the corresponding element in the W matrix is expected to decrease and with it the frequency of the vibrational modes involving such an atom.

In order to find which modes are directly related to the vacancy, we increase the atomic masses of the four n.n. of the vacancy. From the resulting frequency shifts we can identify which frequencies are mainly related to these atoms.

Let us consider figure 5 where we report the Raman spectra of the S_z=0 spin state with 2 different isotopic substitutions. In the former one the mass of the n.n. is increased by 25% (graph in the middle in figure 5) while in the other case by the 100% (graph at the bottom in fig.5). The legend in each graph displays the isotopic mass used.

The Raman spectra can be divided into 4 principal zones labeled as **1-4**.

Zone "**1**" is associated with the vacancy n.n. motion. The main peak in this zone, at ν=1191 cm^{-1}, decreases by $\delta\nu$= 25 cm^{-1} and its intensity decreases from I= 85 a.u. to I= 4 a.u when an isotopic variation of 25% is made.

On the contrary, modes in the region "**2**" of the Raman spectrum are essentially unaffected by the isotopic substitution. The main peak at ν= 821 cm^{-1} shifts by $\delta\nu$= 3 cm^{-1} when the substituting isotopes are the heaviest used (graph at the bottom in the fig.5).

The most intense vibrational mode (labeled as "**3**" in the Raman spectrum) has an intermediate shift from ν=1291 cm^{-1} to ν=1270 cm^{-1} when an atomic

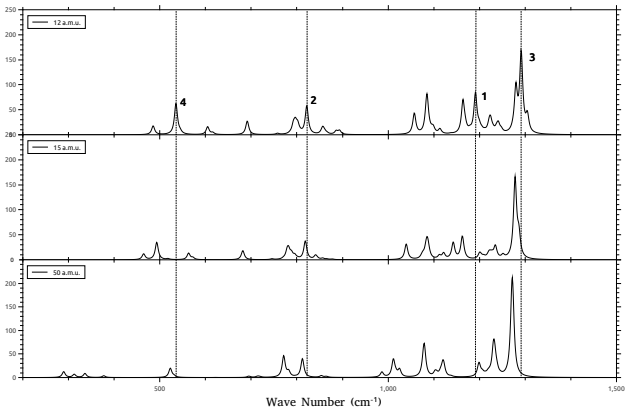

Fig. 5 Raman spectra of the vacancy in the S_z=0 spin state. From the top to the bottom we report the spectra with no isotopic sostitution and with an increasing atomic mass on the first neighbors of the vacancy, as indicated in the legend of each graph. The wave number range varies from 200 cm^{-1} to 1500 cm^{-1} .

mass of 50 a.m.u. is set to the n.n. while its intensity remains the highest one within the Raman spectrum. This confirms that it is a vibrational mode associated with a collective motion of all atoms in the crystal.

Group "**4**" of Raman features is associated to the acoustic phonons created by the vacancy. These modes are directly related to the n.n. as demonstrated by the frequencies shift (about 245 cm^{-1} for the original peak at ν=534 cm^{-1}).

Let us consider now thermodinamic properties such as the zero point energy, heat capacity and entropy. We focus in particular on the difference between the non-defective system and the S_z=0 configuration as a measure of the thermodinamic perturbation due to the defect. This analysis provides important information about relative internal stability of these systems.

We now report the evolution of the entropy (S) and the heat capacity (C_v) when increasing the temperature from 0 K up to 2000 K in the defective and non-defective systems. For the defective system, we consider the S_z=0 spin state in the S_{32} supercell.

Graphs 6 and 7 show that the heat capacity and entropy variation at increasing the temperature in the defective diamond is very similar to the non-defective one. At room temperature and pressure conditions (T= 298.15 K and p= 0.101 MPa) the difference in entropy between non-defective and defective system is 11.0 J mol^{-1} K^{-1}. This difference is mainly due to the numerous low frequency modes which emerge in the defective system. Entropy is indeed proportional to the natural logarithm of the number of possible vibrational configurations of the system.

At room pressure and temperature conditions also the heat capacity in the defective system is higher than that in the non-defective one: a difference of 18.3 J mol^{-1} K^{-1} occurs.

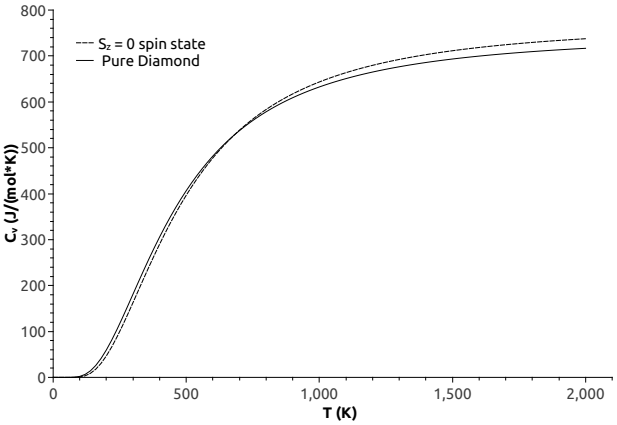

Fig. 6 Heat capacity (C_v) evolution in non-defective and defective diamond as a function of the temperature. The S_{32} supercell in the S_z=0 spin state is considered. Calculations are performed with the B3LYP Hamiltonian .

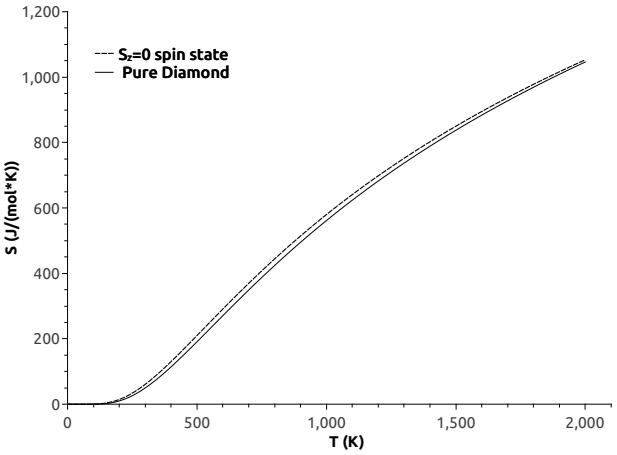

Fig. 7 Entropy (S) evolution in non-defective and defective diamond as a function of the temperature. The S_{32} supercell in the S_z=0 spin state is considered. Calculations are performed with the B3LYP Hamiltonian .

We expect that in the more rigid system the zero point energy is the higher. The non-defective and defective systems differ by 45.2 KJ mol^{-1}, where the non-defective one gives the higher value.

3.1 Anisotropic Displacement Parameters

As anticipated in Section 2.3, an effective way to interpret thermal nuclear motions is that of computing and analyzing atomic ADPs, which quantify mean square atomic displacements in an intuitive way. Indeed, at variance with

vibration normal coordinates, which are collective modes, ADPs allow for an atomic partition of the thermal nuclear motion, providing with a simple graphical tool to discuss such effects, even in complex structures. Furthermore, ADPs can be experimentally derived from X-ray or synchrotron radiation diffraction measurements, thus allowing for validation of the theoretical predictions. The atomic thermal ellipsoids of pure diamond are perfectly spherical and the corresponding ADP has a value which is commonly reported in the range 16.1 - 22.3 10^{-4}Å^2, with a recent accurate determination of 18.1 10^{-4}Å^2 [57]. The *ab initio* evaluation of ADPs requires lattice dynamical calculations to be performed by accounting for phonon dispersion. Within the direct space approach here adopted, increasing the size of the SC in the lattice dynamical calculation corresponds to increasing the sampling of the phonon dispersion within the first Brillouin zone in reciprocal space.

Table 1 Computed ADP (in units of 10^{-4}Å^2) of pure crystalline diamond as a function of the size of the supercell, SC, used for the lattice dynamical calculations, $N_{\rm at}$ being the number of atoms in the SC. The corresponding number n_k of **k**-points over which the FBZ is sampled is also given. A recent experimental determination is reported as a reference [57].

$N_{\rm at}$	n_k	ADP
Exp.		18.1
Interp.	65536	17.7
256	128	16.5
216	108	16.4
128	64	15.9
64	32	15.3
32	16	14.5
16	8	14.2
8	4	11.7
2	1	4.1

The computed ADP of pure diamond at 298.15 K, as obtained by use of equation (8), is reported in Table 1 as a function of the size of the adopted SC. The effect of the inclusion of phonon dispersion is seen to be rather large: a Γ-only calculation (performed on the primitive unit cell containing just $N_{\rm at}$ = 2 atoms) indeed provides an ADP of 4.1 10^{-4}Å^2, which is then systematically increased as the size of the SC increases. Convergence is reached for a SC containing $N_{\rm at}$ = 256 atoms (corresponding to a sampling of the FBZ over 128 **k**-points), as it provides a value of 16.5 10^{-4}Å^2 compared to 16.4 10^{-4}Å^2 that is obtained with a SC with $N_{\rm at}$ = 216 atoms. Without further increasing the size of the SC, a denser sampling of phonon dispersion can then be achieved by Fourier interpolation of the dynamical matrices. Indeed, if in principle, equation (3) could be used to compute and then diagonalize the dynamical matrices of just the $L = \prod_i L_i$ **k**-points defined in Section 2.2, this restriction disappears when long-range electrostatic contributions to the force

constants vanish within the SC (as in the case of diamond). In this case, such an expression can be used to construct the dynamical matrices of a denser set of **k**-points through Fourier interpolation. The ADP obtained by Fourier interpolation (with a corresponding sampling of phonon dispersion over 65536 **k**-points), starting from the largest SC, is 17.7 10^{-4}Å^2, which compares nicely with the accurate experimental reference of 18.1 10^{-4}Å^2 [57], thus confirming the accuracy of the convergence of the lattice dynamical description of the system.

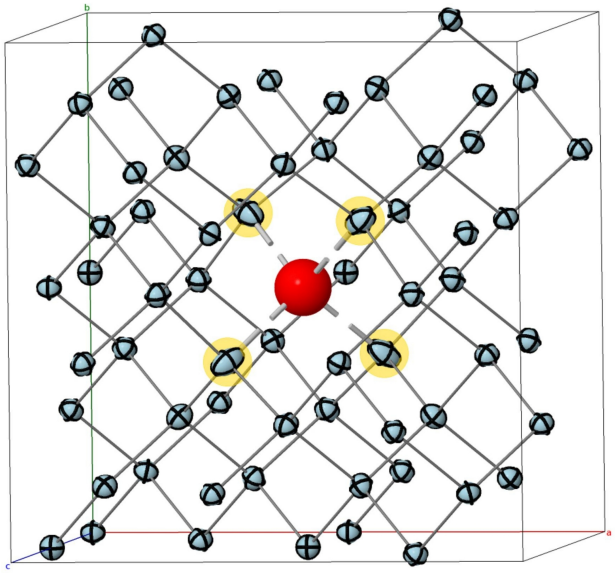

Fig. 8 (color online) Graphical representation of the ADPs (*i.e.* thermal ellipsoids) proper of the 63 carbon atoms surrounding the vacancy (in red) in the 64 centers SC, as computed at 298.15 K. Nearest neighbors of the vacancy are highlighted in yellow.

We shall now analyze the atomic ADPs in defective diamond, that is size, shape and orientation of the thermal ellipsoids of carbon atoms surrounding the vacancy in the lattice. As the vacancy constitutes a local perturbation to the lattice, the features of the ADPs in the vicinity of the defect are found to be almost independent of defect concentration (at least if very high concentrations are not considered). For this reason, we restrict our analysis to the SC containing 64 centers. In Figure 8, a graphical representation is given of all thermal ellipsoids associated with the 63 carbon atoms of the SC. ADPs of atoms sufficiently far apart from the vacancy (represented as a red sphere at the body center of the cell) are seen to be almost perfectly isotropic (*i.e.* spherical), as in the ideal non-perturbed diamond lattice. When carbon atoms close to the vacancy are considered (particularly so for the four nearest neighbors, highlighted in yellow in the figure), the picture is rather different, as the ellipsoids are seen to be quite elongated along the axis connecting each atom

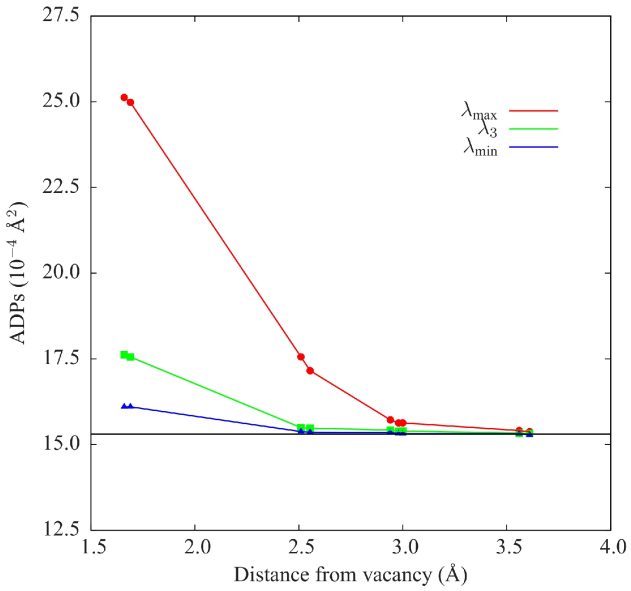

Fig. 9 (color online) The three semi-axes (λ_{max}, λ_{min} and λ_3) of the ADP ellipsoids of carbon atoms as a function of their distance from the vacancy at 298.15 K in the SC containing 64 centers (63 carbons and a vacancy). The horizontal black line marks the value of the isotropic ADP of pure diamond, as obtained from lattice dynamical calculations performed on a SC of the same size.

to the center of the vacancy. In other words, atoms close to the vacancy do exhibit a larger thermal mobility towards the vacancy, as expected.

In order to quantify the perturbation induced by the vacancy on the atomic thermal mobility of the atoms and to analyze up to which distance from the vacancy atoms are actually affected by the vacancy in their thermal motions, we introduce Figure 9. The lengths of the three semi-axes of the thermal ellipsoids (λ_{max}, red circles, λ_{min}, blue triangles, and λ_3, green squares) are reported as a function of the distance of each carbon atom from the vacancy. It is seen that atoms close to the vacancy show a highly anisotropic thermal ellipsoid, with the longest ADP, λ_{max}, almost 56% larger than the shortest one, λ_{min}. Second nearest neighbors (at a distance of about 2.5 Å) are still affected by the vacancy while atoms at distances larger than 3 Åare practically not affected by the vacancy showing a recovered isotropic character of the ADP. The black horizontal line, indeed, marks the isotropic reference value of the ADP of pure diamond with the same SC.

4 Conclusions

References

1. R.B.Jackman (Guest Editor). Special issue on diamond electronics. *Semicond. Sci. Technol.* ***18***, (2003).
2. Robert J. Nemanich, John A. Carlisle, Atsushi Hirata, and Ken Haenen. Cvd diamondresearch, applications, and challenges. *MRS Bulletin*, 39:490–494, 6 2014.
3. A. Hoffman, S. Prawer, and R. Kalsih. Structural transformation of diamond induced by 1-kev ar-ion irradiation as studied by auger and secondary-electron spectroscopies and total-secondary-electron-yield measurements. *Phys. Rev. B* ***45(22)***, 12736,(1992).
4. S. Lagormarsino, P. Olivero, S. Calusi, D. Gatto Monticone, L. Giuntini, M. Massi, S. Sciortino, A. Sytchkova, A. Sordini, and M. Vannoni. Complex refractive index variation in proton-damaged diamond. *Opt. Express* ***20(17)***, 19382,(2012).
5. J. F. Prins. Onset of hopping conduction in carbon-ion-implanted diamond. *Phys. Rev. B* ***31(4)***, 2472,(1985).
6. R. Kalish, A. Reznik, S. Prawer, D. Saada, , and J. Adler. Ion-implantation-induced defects in diamond and their annealing: experiment and simulation. *Phys. Status Solidi A Appl Res* ***174***, 83,(1999).
7. R. Kalish, A. Reznik, K. W. Nugent, and S. Prawer. The nature of damage in ion-implanted and annealed diamond. *Nucl. Instrum. Methods Phys. Res. B* ***148***, 626,(1999).
8. D. J. Twitchen, D. C. Hunt, M. E. Newton, J. M. Baker, T. R. Anthony, and W. F. Banholzer. Electron paramagnetic resonance (epr) and optical absorption studies of defects created in diamond by electron irradiation damage at 100 and 350 k. *Physica B* ***273-274***, 628,(1999).
9. P. F. Laia, S. Prawer, , and C. Noble. Electron spin resonance investigation of ion-irradiated diamond. *Diamond Relat. Mater.* ***11***, 1391,(2002).
10. A. Moro no, S. M. González de Vicente, and E. R. Hodgson. Radiation effects on the optical and electrical properties of cvd diamond. *Fusion Eng. Des.* ***82***, 2563,(2007).
11. H. Amekura and N. Kishimoto. Effects of high-fluence ion implantation on colorless diamond self-standing films. *J. Appl. Phys.* ***104***, 063509,(2008).
12. A. C. Ferrari and J. Robertson. Interpretation of raman spectra of disordered and amorphous carbon. *Phys. Res. B* ***61 (20)***, 14095,(2000).
13. A. C. Ferrari and J. Robertson. Resonant raman spectroscopy of disordered, amorphous, and diamondlike carbon. *Phys. Res. B* ***64 (7)***, 075414,(2001).
14. D. N. Jamieson, S. Prawer, K. W. Nugent, , and S. P. Dooley. Cross-sectional raman microscopy of mev implanted diamond. *Nucl. Instrum. Methods Phys. Res. B* ***106***, 641,(1995).
15. J. D. Hunn, S. P. Withrow, C. W. White, and D. M. Hembree Jr. Raman scattering from mev-implanted diamond. *Phys. Res. B* ***52 (11)***, 8106,(1995).
16. S. Prawer, K. W. Nugent, , and D. N. Jamieson. The raman spectrum of amorphous diamond. *Diamond Relat. Mater.* ***7***, 106,(1998).
17. J. Orwa, K. W. Nugent, S. Prawer, and D. N. Jamieson. Raman investigation of damage caused by deep ion implantation in diamond. *Phys. Rev. B* ***62(9)***, 5461, (2000).
18. R. Brunetto, G. A. Baratta, and G. Strazzulla. Raman spectroscopy of ion irradiated diamond. *J. Appl. Phys.* ***96 (1)***, 380, (2004).
19. P. Olivero, S. Rubanov, P. Reichart, B. C. Gibson, S. T. Huntington, J. R. Rabeau, A. D. Greentree, J. Salzman, D. Moore, D. N. Jamieson, and S. Prawer. Characterization of three-dimensional microstructures in single-crystal diamond. *Diamond Relat. Mater.* ***15***, 1614, (2006).
20. S. Prawer, I. Rosenblum, J. O. Orwa, and J. Adler. Identification of the point defects in diamond as measured by raman spectroscopy: comparison between experiment and computation. *Chem. Phys. Lett.* ***390***, 458, (2004).
21. A. A. Bergman, A. M. Zaitsev, M. Huang, and A.A. Gorokhovsky. Photoluminescence and raman studies of xe ion-implanted diamonds: dependence on implantation dose. *J. Lumin.* ***129***, 1524, (2009).

22. A. M. Zaitsev. *Optical properties of diamond a data handbook*. New York, Springer, (2001).
23. F. Pascale, C. M. Zicovich-Wilson, F. Lòpez Gejo, B. Civalleri, R. Orlando, and R. Dovesi. The calculation of the vibrational frequencies of the crystalline compounds and its implementation in the crystal code. *J. Comp. Chem.*, 25:888–897, 2004.
24. C. M. Zicovich-Wilson, F. Pascale, C. Roetti, V. R. Saunders, R. Orlando, and R. Dovesi. The calculation of the vibration frequencies of α-quartz: The effect of hamiltonian and basis set. *J. Comput. Chem.*, 25:1873–1881, 2004.
25. C. Carteret, M. De La Pierre, M. Dossot, F. Pascale, A. Erba, and R. Dovesi. *J. Chem. Phys.*, 138:014201, 2013.
26. M. Veithen, X. Gonze, and Ph. Ghosez. Nonlinear Optical Susceptibilities, Raman Efficiencies, and Elctro-Optic Tensors from First-Principles Density Functional Perturbation Theory. *Phys. Rev. B*, 71:125107, 2005.
27. L. Maschio, B. Kirtman, R. Orlando, and M. Rérat. Ab initio analytical infrared intensities for periodic systems through a coupled perturbed Hartree-Fock/Kohn-Sham method. *J. Chem. Phys*, 137(20):204113, 2012.
28. L. Maschio, B. Kirtman, M. Rérat, R. Orlando, and R. Dovesi. Ab initio analytical raman intensities for periodic systems through a coupled perturbed Hartree-Fock/Kohn-Sham method in an atomic orbital basis. ii. validation and comparison with experiments. *J. Chem. Phys*, 139(16):164102, 2013.
29. L. Maschio, B. Kirtman, M. Rérat, R. Orlando, and R. Dovesi. Ab initio analytical Raman intensities for periodic systems through a coupled perturbed Hartree-Fock/Kohn-Sham method in an atomic orbital basis. II. Validation and comparison with experiments. *J. Chem. Phys.*, 139:164102, 2013.
30. L. Maschio, B. Kirtman, M. Rérat, R. Orlando, and R. Dovesi. Comment on "ab initio analytical infrared intensities for periodic systems through a coupled perturbed hartree-fock/kohn-sham method" [j. chem. phys. 137, 204113 (2012)]. *J. Chem. Phys.*, 139:167101, 2013.
31. M. Ferrero, M. Rérat, R. Orlando, and R. Dovesi. The Calculation of Static Polarizabilities of Periodic Compounds. The Implementation in the CRYSTAL Code for 1D, 2D and 3D Systems. *J. Comput. Chem.*, 29:1450–1459, 2008.
32. M. Ferrero, M. Rérat, R. Orlando, and R. Dovesi. *J. Chem. Phys.*, 128:014110, 2008.
33. P. Baranek, C. M. Zicovich-Wilson, C. Roetti, R. Orlando, and R. Dovesi. Well Localized Crystalline Orbitals Obtained from Bloch Functions: The Case of $KNbO_3$. *Phys. Rev. B*, 64:125102, 2001.
34. Y. Noël, C. M. Zicovich-Wilson, B. Civalleri, Ph. D'Arco, and R. Dovesi. Polarization Properties of ZnO and BeO: An *Ab initio* Study through the Berry Phase and Wannier Functions Approaches. *Phys. Rev. B*, 65:014111, 2002.
35. C. M. Zicovich-Wilson, J. Torres, F. Pascale, L. Valenzano, R. Orlando, and R. Dovesi. The *Ab Initio* Simulation of the IR Spectra of Pyrope, Grossular and Andradite. *J. Comput. Chem.*, 29:2268–2278, 2008.
36. J. Baima, M. Ferrabone, R. Orlando, A. Erba, and R. Dovesi. Thermodynamics and phonon dispersion of pyrope and grossular silicate garnets from ab initio simulations. *Phys. Chem. Minerals*, 2015. submitted.
37. K. Parlinski, Z. Q. Li, and Y. Kawazoe. First-principles determination of the soft mode in cubic zro_2. *Phys. Rev. Lett.*, 78:4063–4066, May 1997.
38. A Togo, F Oba, and I Tanaka. First-principles calculations of the ferroelastic transition between rutile-type and cacl2-type sio2 at high pressures. *Phys. Rev. B*, 78:134106, Oct 2008.
39. A. Erba, M. Ferrabone, R. Orlando, and R. Dovesi. Accurate dynamical structure factors from ab initio lattice dynamics: The case of crystalline silicon. *J. Comput. Chem.*, 34:346, 2013.
40. A. Erba, M. Shahrokhi, R. Moradian, and R. Dovesi. On how differently the quasi-harmonic approximation works for two isostructural crystals: Thermal properties of periclase and lime. *J. Chem. Phys.*, 142:044114, 2015.
41. A. Ø. Madsen, B. Civalleri, M. Ferrabone, F. Pascale, and A. Erba. Anisotropic displacement parameters for molecular crystals from periodic hartree-fock and density functional theory calculations. *Acta Cryst. A*, 69:309, 2013.

42. A. Erba. *J. Chem. Phys.*, 141:124115, 2014.
43. J. D. Dunitz, V. Schomaker, and K. N. Trueblood. *J. Phys. Chem.*, 92:856, 1988.
44. A. Erba, J. Maul, R. Demichelis, and R. Dovesi. Assessing thermochemical properties of materials through ab initio quantum-mechanical methods: The case of α-al$_2$o$_3$. *Phys. Chem. Chem. Phys.*, 17:11670–11677, 2015.
45. A. Erba, J. Maul, M. De La Pierre, and R. Dovesi. Structural and elastic anisotropy of crystals at high pressure and temperature from quantum-mechanical methods: The case of mg$_2$sio$_4$ forsterite. *J. Chem. Phys.*, 142:204502, 2015.
46. A. Erba, J. Maul, M. Itou, R. Dovesi, and Y. Sakurai. Anharmonic thermal oscillations of the electron momentum distribution in lithium fluoride. *Phys. Rev. Lett.*, 2015. in press.
47. Axel D Becke. Density-functional thermochemistry. iii. the role of exact exchange. *J. Chem. Phys.*, 98(7):5648–5652, 1993.
48. Roberto Dovesi, Roberto Orlando, Alessandro Erba, Claudio M. Zicovich-Wilson, Bartolomeo Civalleri, Silvia Casassa, Lorenzo Maschio, Matteo Ferrabone, Marco De La Pierre, Philippe D'Arco, Yves Nol, Mauro Caus, Michel Rrat, and Bernard Kirtman. Crystal14: A program for the ab initio investigation of crystalline solids. *Int. J. Quantum Chem.*, 114(19):1287–1317, 2014.
49. R. Dovesi, V. R. Saunders, C. Roetti, R. Orlando, C. M. Zicovich-Wilson, F. Pascale, B. Civalleri, K. Doll, N. M. Harrison, I. J. Bush, Ph. D'Arco, and M. Llunell. *CRYSTAL 2014 User's Manual*. University of Torino, Torino, 2013.
50. J. S. Binkley, J. A. Pople, and W. J. Hehre. Self-consistent molecular orbital methods. 21. small split-valence basis sets for first-row elements. *J. Am. Chem. Soc.*, 102,(1980).
51. D.S.Knight and W.B.White. *J. Mater. Res.* ***4***, 385, (1989).
52. P.Ugliengo, B.Civalleri, C.M. Zicovih-Wilson, and R.Dovesi. *Chem. Phys. Lett.* ***318***, 247, (2000).
53. M.Catti, P.Ugliengo, and B.Civalleri. *Chem. Phys. B* ***104***, 7259, (2000).
54. P.Baranek, A. Lichanot, R.Orlando, and R.Dovesi. *Chem. Phys. Lett.* ***340***, 362, (2001).
55. D.N.Jamieson, S.Prawer, K.W.Nugent, and S.P.Dooley. *Nucl. Instr. and Meth. in Phys. Res. B*, 106, (1995).
56. J.F. Ziegler, J.P. Biersack, and M.D. Ziegler. *The Stopping and Range of Ions in Matter*, SRIM Co., (2008).
57. Niels Bindzus, Tine Straasø, Nanna Wahlberg, Jacob Becker, Lasse Bjerg, Nina Lock, Ann-Christin Dippel, and Bo B. Iversen. Experimental determination of core electron deformation in diamond. *Acta Crystallographica Section A*, 70(1):39–48, 2014.